The Astrophysical Journal, 604:187–195, 2004 March 20

NUMERICAL SIMULATIONS OF LOCAL SHOCK REFORMATION AND ION ACCELERATION IN SUPERNOVA REMNANTS

R. E. Lee and S. C. Chapman
Space and Astrophysics Group, Physics Department, University of Warwick, Coventry CV4 7AL, UK; leer@astro.warwick.ac.uk

and

R. O. Dendy
UKAEA Culham Division, Culham Science Centre, Abingdon, Oxfordshire OX14 3DB, UK
Received 2003 September 16; accepted 2003 December 8

ABSTRACT

The identification of preacceleration mechanisms for cosmic rays in supernova remnant shocks is an outstanding problem in astrophysics. Recent particle-in-cell (PIC) shock simulations have shown that the inclusion of the full electron kinetics yields non–time-stationary solutions, in contrast to previous hybrid (kinetic ions, fluid electrons) simulations. Here, by running a PIC code at high phase space resolution, we identify a new ion acceleration mechanism associated with the time dependence of the shock. From simple scaling arguments, these results suggest that for realistic parameters at supernova remnant shocks, such as an inflow speed of around 2.5×10^7 m s^{-1}, an accelerated ion population is created at energies of order 10–20 MeV. These simulations indicate the importance of capturing the full self-consistent plasma dynamics in order to study preacceleration.

Subject headings: acceleration of particles — cosmic rays — methods: numerical — shock waves — supernovae: general — supernova remnants

1. INTRODUCTION

Protons form the majority constituent of Galactic cosmic rays; however, the mechanism for their initial acceleration remains an outstanding problem in astrophysics. Supernova remnants (SNRs) provide the most likely source of kinetic energy to sustain the cosmic-ray population, and local acceleration of electrons has been indirectly observed at the expanding shock front of SNRs (see, e.g., Koyama, Petre, & Gotthelf 1995). It is widely accepted that ions should also be accelerated at these sites; however, until recently a firm observational link between supernova remnants and locally accelerated ions has been lacking. X-ray and γ-ray data from supernova remnant RX J1713.7−3946 (see, e.g., Enomoto et al. 2002) shows energy spectra that can only be explained by accelerated ions. Several mechanisms are postulated to accelerate particles at SNR shocks. Fermi acceleration (Fermi 1949), which arises as a particle repeatedly scatters off turbulent structures on either side of the shock, is in principle capable of accelerating ions to these high energies (Bell 1978). However, to work effectively, a suprathermal initial energy population is required so that particles can recross the shock front (Jokipii 1987). Identifying preacceleration mechanisms that can initiate the energization of completely nonrelativistic ions is an important problem. A candidate mechanism is introduced in the present paper.

The Rankine-Hugoniot relations (Tidman & Krall 1971) can be used to determine the discontinuity in parameters across a collisionless shock: that is, a shock in which the particle mean free path is much greater than length scales of interest. They are derived from magnetohydrodynamic (MHD) conservation equations in the limit away from the shock. Further conditions are imposed by the fact that a shock must also increase entropy, so that no subsonic flow can spontaneously become supersonic. For an Alfvénic Mach number $M_A \gtrsim 3$, the shock is supercritical in that the increase in entropy, and in ion heating, required by the Rankine-Hugoniot relations is achieved via the ion kinetics; at least in part, by reflection of a fraction of upstream ions at the shock. A generic supercritical, quasi-perpendicular, collisionless shock in which ions reflect and gyrate in a foot region upstream has been suggested by hybrid (particle ions, fluid electrons) simulations (see, e.g., Quest 1985, 1986; Burgess, Wilkinson, & Schwartz 1989) and confirmed by in situ observations of the Earth's bow shock (see, e.g., Sckopke et al. 1983).

To study the acceleration of electrons, their full kinetics are needed, which requires the use of a particle-in-cell (PIC) code. Electron acceleration in the parameter regime relevant to SNRs has been studied using PIC codes by, for example, Hoshino & Lembège (1995), Bessho & Ohsawa (1999), Dieckmann et al. (2000), Shimada & Hoshino (2000), and Schmitz, Chapman, & Dendy (2002a, 2002b). Importantly, inclusion of the full electron kinetics significantly alters the dynamics of the shock. In contrast to the static solutions obtained in hybrid simulations, the PIC simulations reveal a dynamic, reforming shock structure (Lembège & Savoini 1992; Schmitz et al. 2002b; Scholer, Shinohara, & Matsukiyo 2003). It follows that in studies of ion acceleration at shocks, as in the present paper, retention of full electron kinetics is desirable in order to resolve fully the shock dynamics (see also Scholer et al. 2003). Here we present results of PIC code simulations that have high resolution in real space and phase space, over relatively long run times, for parameters relevant to SNR shocks. These show that the time-dependent electromagnetic fields at the reforming shock can accelerate ions from background to suprathermal energies, thus providing a natural mechanism for ion injection.

2. SIMULATION

We use a relativistic electromagnetic PIC code to simulate the structure and evolution of a supercritical, collisionless,

perpendicular magnetosonic shock. In a PIC simulation the distribution functions of both ions and electrons are represented by computational superparticles, whilst the electromagnetic fields are defined on a grid in configuration space. Particle trajectories are evolved from the fields via the Lorentz force, then the fields are evolved from the new particle positions via Maxwell's equations (Birdsall & Langdon 1991). The code we use to simulate the shock is based on that described in Devine, Chapman, & Eastwood (1995) and has been used recently to examine electron acceleration in SNR shocks (Dieckmann et al. 2000; Schmitz et al. 2002a, 2002b). All vector fields, bulk plasma properties, and particle velocities are a function of one configuration space coordinate (x), and time. This simplification enables detailed phase space resolution for relatively long run times. PIC simulations in two spatial dimensions (see, e.g., Lembège & Savoini 1992) yield overall shock dynamics that are in agreement with the results seen here.

In common with Shimada & Hoshino (2000) and Schmitz et al. (2002a, 2002b), we use the piston method (see, e.g., Burgess et al. 1989 and references therein) to set up the shock. Particles are injected on the left-hand side of the simulation box with a drift speed $v_{\rm inj}$ and with a random thermal velocity $u_{\rm therm}$ derived from the upstream temperature $T_1 = T_{i,1} = T_{e,1}$ via $u_{\rm therm} = (kT_1/m)^{1/2}$, where the indices "1" and "2" refer to upstream and downstream, respectively; here "i" refers to ions, "e" to electrons, m is the particle mass, and k denotes Boltzmann's constant. On the boundary at which the particle injection takes place, the magnetic field ($B_{z,1}$) is constant and the electric field ($E_{y,1}$) is calculated self consistently. The right-hand boundary is taken to be a perfectly conducting, perfectly reflecting wall. Particles reflect off this boundary, and a shock then forms, propagating to the left through the simulation box; sufficient time is allowed for the shock to propagate sufficiently far upstream that the boundary conditions are no longer important. The size of a grid cell is defined as a Debye length ($\lambda_{\rm D}$), and the time step to less than $\lambda_{\rm D}/c$, for numerical stability reasons (Hockney & Eastwood 1981). In our simulations, $u_{\rm therm} \ll v_{\rm inj}$, so that the speed of incoming ions perpendicular to the magnetic field can be approximated by $v_{\rm inj}$; thus, the ion Larmor radius is simply $\lambda_{ci} \simeq v_{\rm inj}/\omega_{ci}$, where ω_{ci} is the ion cyclotron frequency. We use a simulation box of $\sim$30 ion upstream Larmor radii (λ_{ci}), that is, 15,000 or 30,000 grid cells, depending upon mass ratio and Alfvénic Mach number. The superparticle density is $\sim$200 per species per cell to ensure good resolution in phase space. In this configuration, the time taken by the shock to traverse the simulation box acts as a limiting time for a simulation. To enable the shock and particle dynamics to be followed over extended timescales, whilst retaining high particle density, a simple shock following algorithm is implemented. This holds the peak in magnetic field at 8 λ_{ci} from the left-hand boundary (Schmitz et al. 2002a, Appendix A). This distance is chosen so that no particles that are reflected off the shock subsequently reach the upstream boundary, whilst it leaves a significant amount of the simulation box (around 20 λ_{ci}) downstream.

Here results are presented from simulation runs of perpendicular shocks propagating into a magnetic field ($B_{z,1}$) of 1×10^{-7} tesla, which is consistent with range of values expected at supernova remnants (see, e.g., Ellison & Reynolds 1991). The ratio of electron plasma frequency to electron cyclotron frequency is $\omega_{pe}/\omega_{ce} = 20$, and the upstream ratio of plasma thermal pressure to magnetic field pressure is $\beta = 0.15$. The shock has an Alfvénic Mach number ($M_{\rm A}$) of 10.5 and a simulation mass ratio of ion mass to electron mass ($M_R = m_i/m_e$) of 20 (in common with Shimada & Hoshino 2000; Schmitz et al. 2002a, 2002b); this reduced mass ratio is necessary to enable ion and electron timescales to be captured within the same simulation, with reasonable computational overheads. Although artificially small mass ratios can lead to small values of ω_{pe}/ω_{ce}, which could in turn lead to artificial reformation, it has been established using realistic mass ratios (Scholer et al. 2003) that this reformation is not a computational artifact. As we shall see, these parameter values can be scaled to those expected in supernova remnants.

3. RESULTS

The key phenomenology found in these PIC simulations arises from the non–time-stationary nature of the reforming shock. This is shown in Figure 1, which plots magnetic field strength as a function of x and time. As with all figures in this paper, this is presented in a frame where the downstream plasma is at rest, using data collected from a segment of the simulation run where the shock has formed and is propagating independently of the boundary conditions. The shock can be seen to move upstream, from the right to the left of the simulation box, over time, with the peaks in magnetic field (the shock ramp) recurring on the timescale of the local ion cyclotron period. Over the course of each cycle the ramp forms first, then a foot region grows in front of the stationary shock ramp, whilst the shock strength is maximal. The shock structure then collapses and a new ramp (magnetic field peak) forms $\sim 2\lambda_{ci}$ upstream, and a new cycle starts. The shock thus propagates upstream (left) in a stepwise fashion.

In our PIC simulations the shock and its accompanying electromagnetic fields are thus time dependent. However, time independence is an assumption used to derive the Rankine-Hugoniot relations, so that the Rankine-Hugoniot relations will only apply far upstream and downstream of the shock. We find that the instantaneous shock speed $u_s(t)$ oscillates in the range $[0, 3\langle u_s \rangle]$; here $\langle u_s \rangle = 1 \times 10^7$ m s^{-1} $= 3.5 v_a$, where v_a denotes the upstream Alfvén speed, is the time averaged shock speed in the downstream plasma rest frame. The magnetic field reaches a peak of $10B_{z,1}$, or 1×10^{-6} T. However, looking on longer spatiotemporal scales, the average shock speed $\langle u_s \rangle$ is equivalent to the value predicted from Rankine-Hugoniot, and the average magnetic field strength downstream is also consistent.

Let us now examine the ion phase space. Figures 2, 3, and 4 show snapshots of the spatial distributions of ion particle properties and the corresponding magnetic fields and potentials, at three different stages of the reformation cycle whose time and space coordinates are displayed in Figure 1 by the three black lines denoted "A," "B," and "C."

Figure 2 shows a snapshot at time $t = 4\omega_{ci}$. Ions flow in from the left-hand injection boundary at $v_{\rm inj}$, until they reach the shock front (currently situated at 38 λ_{ci}). At this stage of the reformation cycle the shock front is almost stationary (see Fig. 1), and the presence of the "ramp" in the magnetic field and its accompanying potential leads to the specular reflection of a fraction of the incident ions. Consistent with a shock at rest in this frame, the ions simply reflect with $v_x \rightarrow -v_x$. These then move upstream into a region in front of the shock, the "foot" region (ions labeled "A"). The reflected ions form a relatively energetic population, as shown on the ion energy

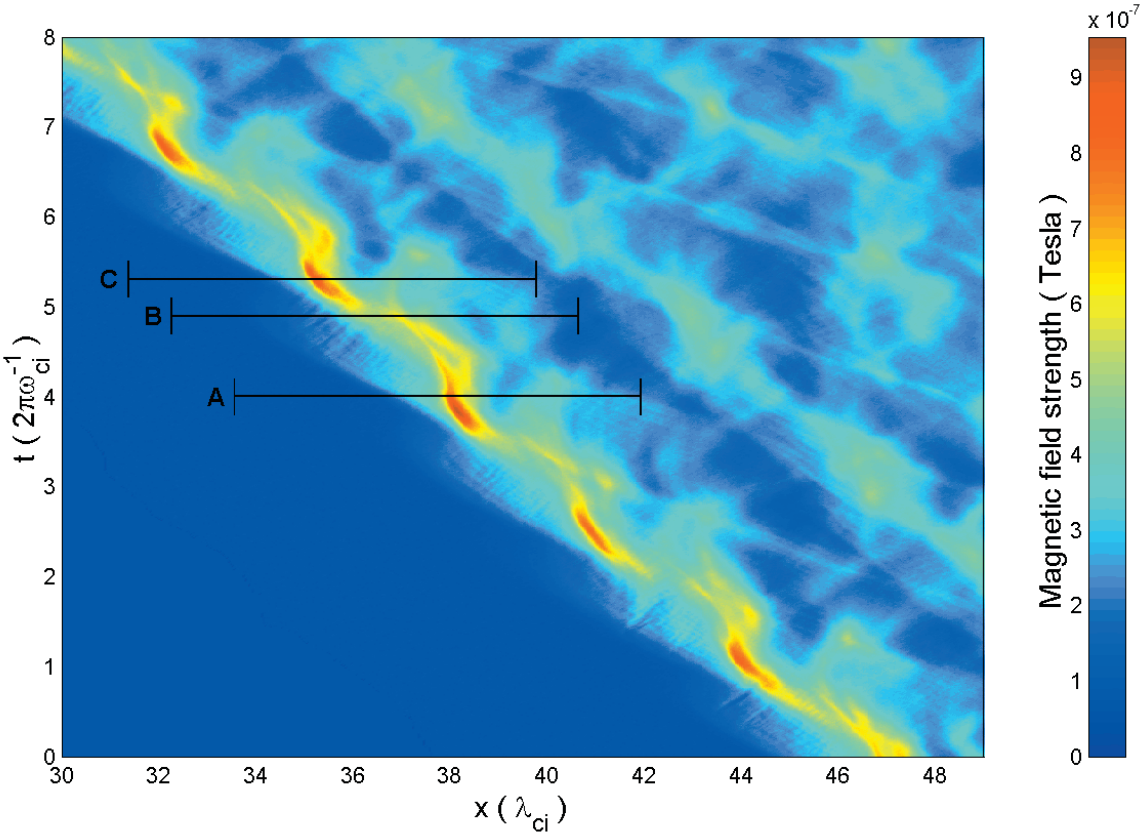

FIG. 1.—Evolution of perpendicular magnetic field strength, over time (*vertical axis*, in units of upstream ion cyclotron period, $2\pi\omega_{ci}^{-1}$), and space (*horizontal axis*, normalized to $\lambda_{ci} = v_{\rm inj}/\omega_{ci}$); here $v_{\rm inj}$ is the injection velocity and ω_{ci} the upstream ion cyclotron frequency. The spatiotemporal positions of the simulation snapshots in Figs. 2, 3, and 4 are labeled "A," "B," and "C," respectively.

plot, where their energies are dispersed from 1 to 6 times their injection energy. They are effectively trapped in a potential well by their low velocities in x, with their main energy gain arising from an increase in y-velocity.

Moving further through the shock reformation cycle, Figure 3 shows a snapshot at $t = 4.9\omega_{ci}$. Starting with the magnetic field, we see that the ramp region is now less well defined (see also Fig. 1). In the ion phase space there is no clear foot population; instead, ions are now starting to gyrate back toward the shock and move downstream to form the population labeled "B." On traveling back toward the shock, velocity is transferred from y to x as the ions gyrate around the magnetic field lines; thus, the y-velocity declines and, downstream, appears to oscillate. The energies of the ions in population "B" are dispersed in energy.

By $t = 5.3\omega_{ci}$, as shown in Figure 4, a new ramp has formed and the reflected ions are beginning to form a new foot region as the next cycle commences. Figure 4 shows both populations of ions; the ions that specularly reflect to form the foot (population "A"), and those energized and leaving the foot to flow downstream (population "B"). Referring back to Figure 1, we see that a new shock has formed and is again nearly stationary in this frame.

This supercritical shock foot-ramp structure, with specularly reflecting ions contributing to collisionless ion heating at the shock, has been established via hybrid simulations (see, e.g., Leroy 1983, Burgess et al. 1989, and references therein). The hybrid description treats the electrons as a massless charge neutralizing fluid, so that a prescription is needed for the electron resistivity. This can affect whether time stationary solutions are observed: as noted by Quest (1986), hybrid simulations can generate time-stationary or shock reforming solutions, depending upon the choice of resistive diffusion length and the simulation grid size. For example, Quest (1986) performed hybrid simulations at high Mach numbers and found reforming shock structures; whereas Leroy (1983) and Burgess et al. (1989) at lower Mach numbers and with a differing resistivity, obtained a time-stationary shock solution.

This implies that although the overall features of the foot-ramp structure are not sensitive to the resistivity and are adequately described by hybrid codes, the dynamics, and particularly the shock reformation processes, can be sensitive. The PIC representation, which includes the full electron kinetics, is needed to unambiguously capture these features, and their consequences for ion acceleration, which we will discuss next.

3.1. *Specular Reflection and Upstream Frame Transformations*

The foot region of the shock is formed from ions that undergo specular reflection off the shock front. Consider an ion approaching the shock at a speed u_1 with respect to the rest frame of the downstream plasma. If the shock were time-stationary and simply propagating to the left with speed u_s, then we could move into a frame where the shock is at rest, as shown in Figure 5, by applying a transform to all velocities of $-u_s = -\langle u_s \rangle = -u_s(t)$. In this shock rest frame, ions upstream of the shock approach it with speed $u_i' = u_i - u_s$ and undergo reflection in which their energy is conserved, so

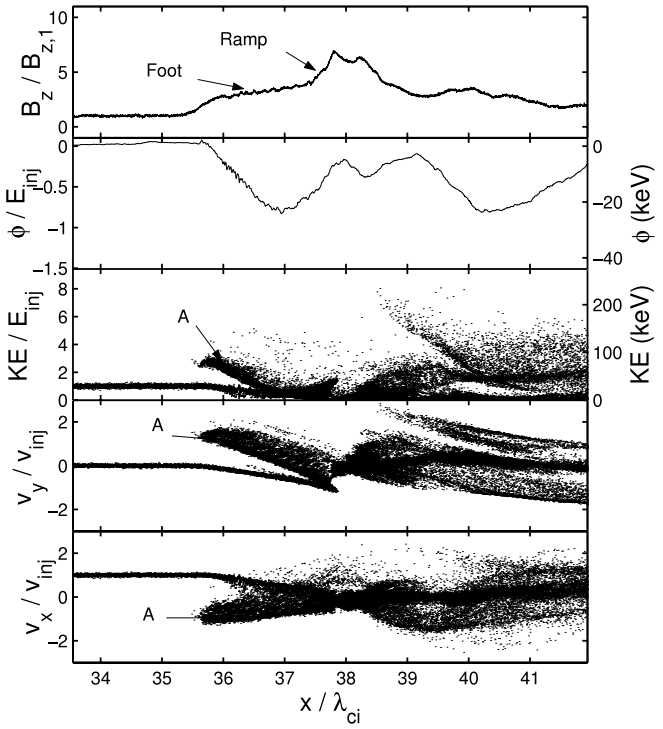

FIG. 2.—Spatial cross section of the simulation in the shock region at $t = 4.0\omega_{ci}$, corresponding to line A in Fig. 1. The top panel shows perpendicular magnetic field, normalized to the upstream value $B_{z,1}$. The second panel shows the potential in units normalized to the ion injection energy ($E_{\rm inj}$) on the left-hand side, and in keV on the right. The middle panel shows the kinetic energy of the ions again normalized to $E_{\rm inj}$ and keV. The fourth panel from top shows the ion velocity in the y direction (perpendicular both to the shock normal and the magnetic field) normalized to injection velocity ($v_{\rm inj}$). The bottom panel shows the ion phase space (x vs. v_x) with velocities normalized to $v_{\rm inj}$. The feature "A" in the three lower panels relates to foot formation by shock-reflected ions.

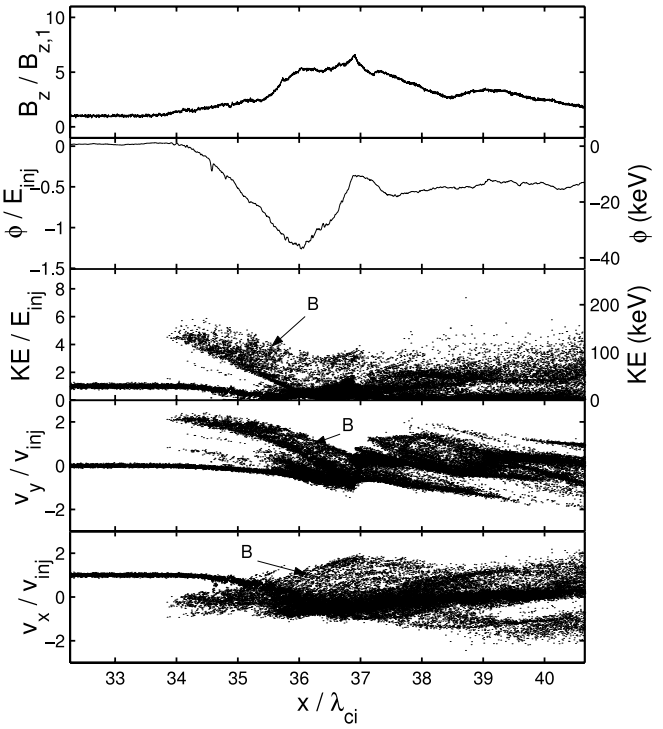

FIG. 3.—Spatial cross section of the simulation in the shock region at $t = 4.9\omega_{ci}$, corresponding to line B in Fig. 1. The axes are as in Fig. 2. The feature "B" in the three lower panels relates to energized reflected ions whose Larmor orbits carry them back toward the shock.

that after reflection, ions move with velocity $u_r' = -u_i'$. To transform back to the frame in which the shock is moving at u_s, we apply the transform in reverse, so that reflected ions now move at $u_r = u_r' + u_s = -u_i + 2u_s$. Thus, with respect to the downstream rest frame, specular reflection in the time-stationary shock rest frame constitutes an acceleration mechanism.

Now let us turn to the time-dependent situation that arises in our simulations, where $u_s(t) \neq \langle u_s \rangle$ and the shock is reforming, as shown in Figure 6. Although in general the shock is highly nonstationary, we can, to good approximation, consider the time interval when the shock has formed and is approximately at rest in the downstream rest frame (see Fig. 1) as defining an inertial frame, and we note that most of the ion reflection occurs during this time period (see Figs. 2, 3, and 4). Consequently, at times of maximum particle reflection in our simulations, the shock is at rest, so transformations to and from the shock rest frame, and specular reflection in it, involve no changes in particle speed. Thus, specular reflection does not in this case represent an acceleration mechanism.

We can see this in the ion phase space plots in Figures 2 and 4, which show specular reflection in the downstream rest frame. Ions are incident at the shock with velocities $v_{\rm inj}$, and those that are reflected have velocities around $-v_{\rm inj}$. The ions reflect off the shock ramp and form a foot region, so that the overall shock structure is unchanged, but particles no longer gain energy by specular reflection. However, ions are still

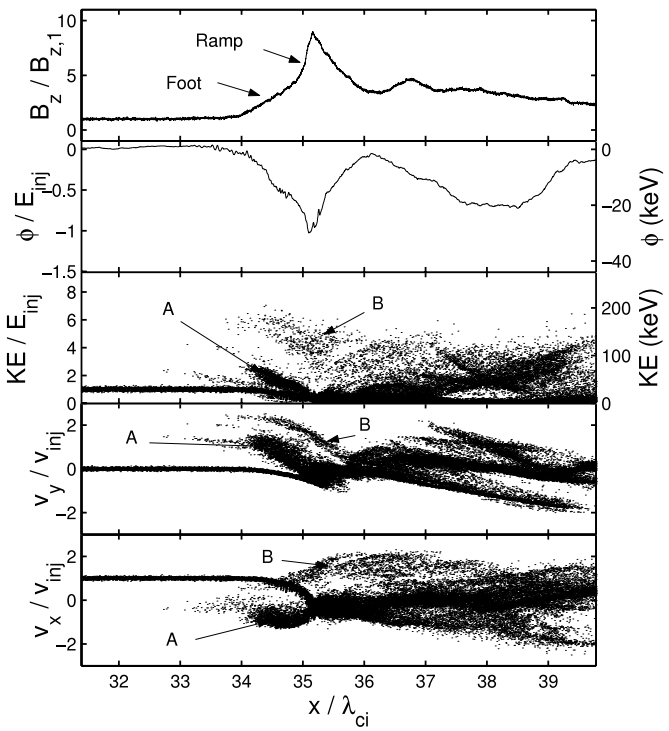

FIG. 4.—Spatial cross section of the simulation in the reformed shock region at $t = 5.3\omega_{ci}$, corresponding to line C in Fig. 1. The axes are as in Fig. 2. Both reflected ions reforming the foot (A), and energized ions passing through the shock (B), are visible.

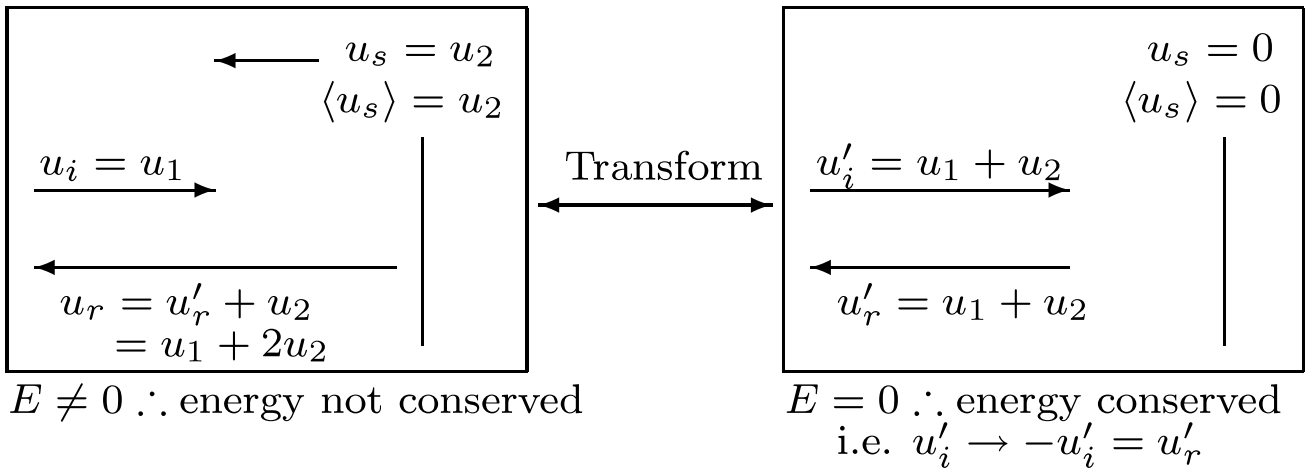

FIG. 5.—Specular reflection of upstream ions at a uniformly moving time stationary shock front, seen in the rest frame of the downstream plasma (*left*) and of the shock itself (*right*).

accelerated in the foot region, and some eventually gain up to 6 times their injection energies, as seen in Figure 7, where snapshots of normalized ion kinetic energy are shown at times of maximum ion energization for a variety of simulation parameters. The nature and scaling of this energization will now be discussed.

3.2. *The Shock Foot Potential as an Acceleration Mechanism*

Let us now consider the dynamics of suprathermal ions, that is, those ions that acquire significantly higher energies than the majority. We have selected a group of ions that have final energies $\gtrsim 6$ times the injection ion energy; these are close to the maximal energies reached, and there exists a continuum of energies from zero up to these values. The paths of these particles have been traced though the simulation and are found to be very similar, with little dispersion in phase space as they pass through the shock. Figure 8 shows a few of these particle trajectories. The essential features of the time dependent electromagnetic fields in this topology can be captured by plotting the potential $\phi(x,t) = \int E_x dx$, and this is also shown in Figure 8 as a contour plot. We can see both the bulk potential that spans the foot region and oscillates on the timescale for shock reformation, that is, ω_{ci}^{-1}, and also finer scale structures. The latter correspond to electron phase space holes that form along the inflow edge of the bulk potential, at the edge of the foot region. These small short-lived potential wells have been shown to be linked to electron acceleration at shocks (Schmitz et al. 2002b).

We might expect ion, as opposed to electron, spatial and temporal scales to dominate these bulk electromagnetic fields, and this is discussed in the Appendix. We see from Figure 8 that the ions are not strongly perturbed by the finer, electron scale structure and instead follow that of the bulk potential which essentially follows the field gradients and the ion Lorentz force (eqs. [A12] and [A15]).

Comparing the electron acceleration, as seen in Schmitz et al. (2002b), with the ion acceleration described here, one notes that the nature, timescales, and magnitude of the energization are markedly different. Acceleration of electrons occurs in two stages, prior to and during the their interaction with the shock front. A fast acceleration phase occurs when the electrons interact with strongly nonlinear plasma structures that combine features of electrostatic solitary waves, electron phase space holes, and ion acoustic solitons. These structures arise on electron spatial scales, and occur toward the leading edge of the bulk potential well. This phase is followed by a slower, roughly μ-conserving, acceleration phase, as the electron navigates the ramp region of the shock. In contrast, ion acceleration occurs after reflection from the shock front, whilst the ion is in the foot region. This is a much slower process than the electron acceleration, and it takes place on spatiotemporal scales that are governed by the ion gyromotion.

The magnitude of energization is also different for ions and electrons. In the simulations presented here, ions achieve a consistent maximal energization of around 6 times injection energy. In the simulations reported in Schmitz et al. (2002b), electrons are seen at over 50 times their injection energies.

The particle trajectories initially meet the shock at a time $t = 3.7\omega_{ci}^{-1}$, when the magnetic field is at its strongest (Fig. 1) and the potential well at its narrowest (Fig. 8). They are reflected off the shock front and move back upstream into the foot region. Over the course of an ion cyclotron period the ions then gyrate back toward the shock. Whilst in the foot

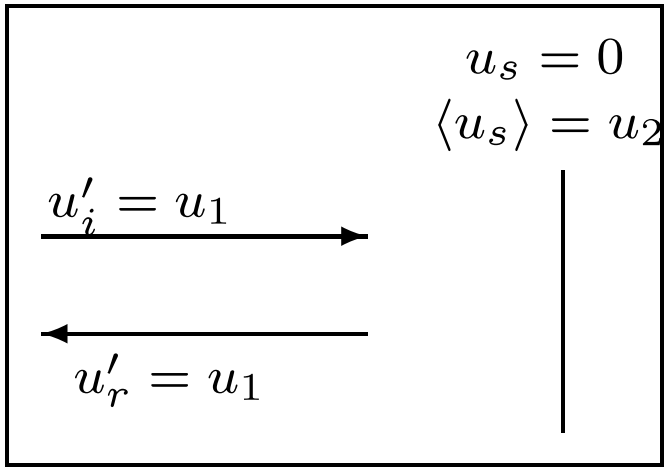

FIG. 6.—Specular reflection of upstream ions at an instantaneously stationary reforming shock.

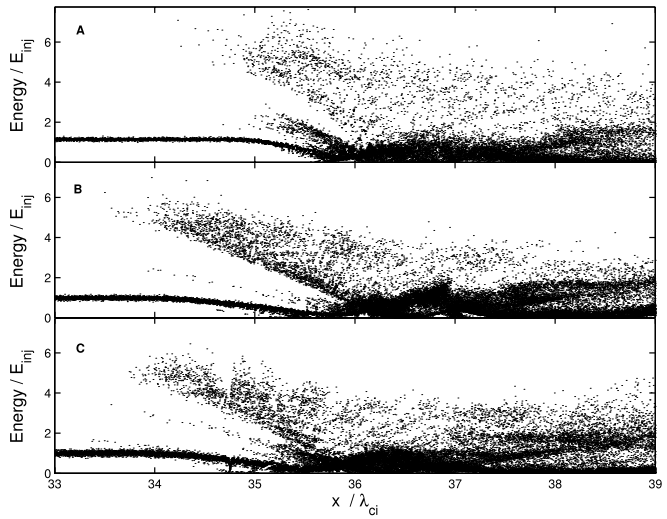

FIG. 7.—Spatial distribution of normalized ion energies in the downstream frame, at the time of maximum energization, from three different simulations. Panels show (*a*) results from the $M_A = 21$, $M_R = 20$ simulation, (*b*) the $M_A = 14.5$, $M_R = 40$ simulation, and (*c*) the $M_A = 10.5$, $M_R = 20$ simulation. Energization up to 6 times the initial energy is visible in all of the cases.

region the ions gain energy (see Fig. 4). At their second interaction with the shock side of the potential well, ions pass through the shock, because the energy gained in the foot region is too high for them to be reflected. Thus, the ion cyclotron period places a limit on the energy gain that is possible by this process, as reflected ions cannot be trapped in the well for more than one cyclotron gyration because of their increased energy.

In summary, specular reflection creates a population of ions at $\sim m_i v_{\rm inj}^2/2$ that begin forming the foot region. These ions move with the expanding potential well as the foot region grows (Fig. 8). This potential then collapses, expelling these ions into the downstream region, energizing them, and creating a population (Fig. 4, "B") dispersed in energy and extending up to $\sim 6 \times m_i v_{\rm inj}^2/2$.

From the above discussion, one can infer the characteristic timescales governing ion acceleration. We consider a scaling of parameters, such as $m \rightarrow m'$, $\boldsymbol{B} \rightarrow \boldsymbol{B}'$, $v_{\rm inj} \rightarrow v'_{\rm inj}$, provided that a reforming shock solution still exists for the new parameter regime.

From Figures 1 and 8 the characteristic timescale of shock reformation (T) and length scale of the foot region (L) are

$$T \simeq 1/\omega_{ci}, \tag{1}$$

$$L \simeq v_{\rm inj}/\omega_{ci}. \tag{2}$$

After acceleration, the ions are still nonrelativistic (Figs. 2, 3, and 4), so that kinetic energy is just $E = mv^2/2$. If we now consider a new set of parameters, $L \rightarrow L'$, $T \rightarrow T'$, corresponding to $m \rightarrow m'$, $\boldsymbol{B} \rightarrow \boldsymbol{B}'$, $v_{\rm inj} \rightarrow v'_{\rm inj}$, then the following scaling holds:

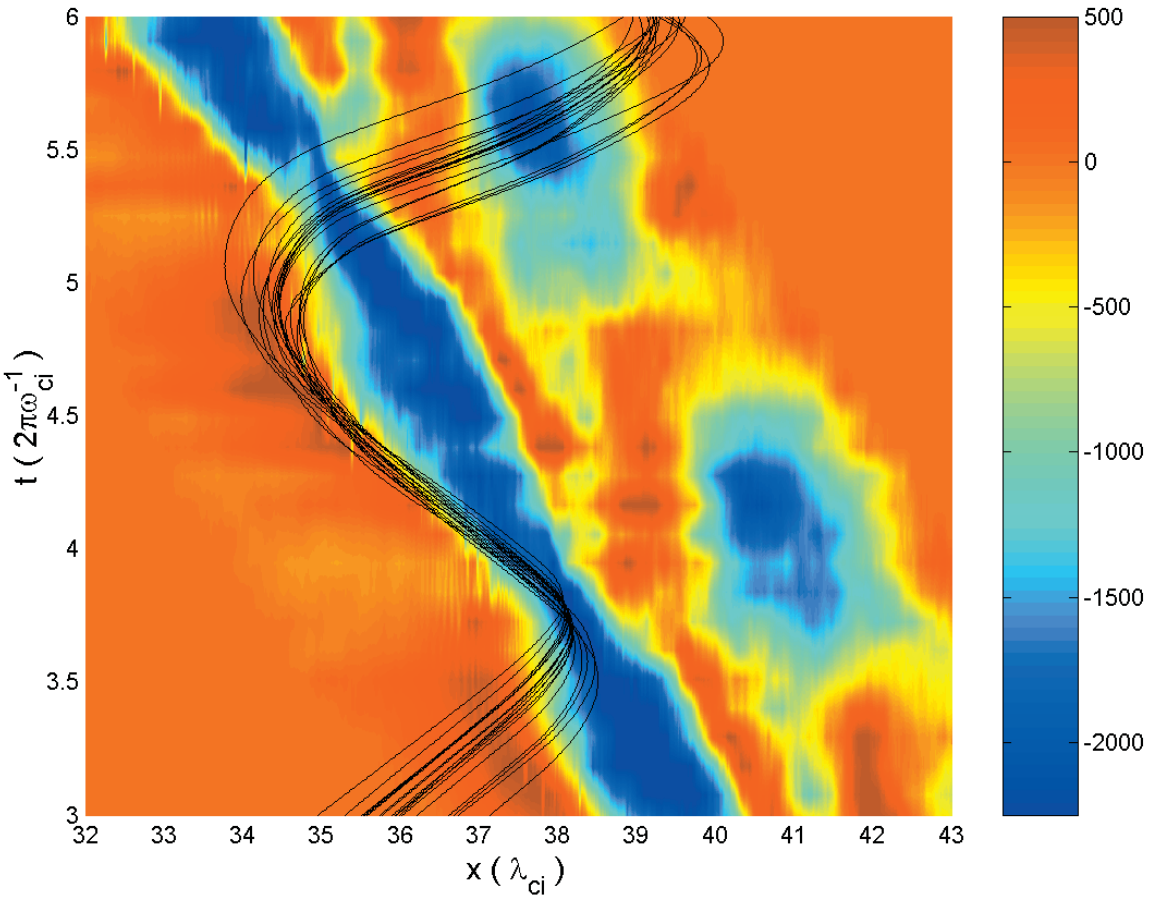

FIG. 8.—Potential in volts (*values in color bar*) over time (*vertical axis*) and space (*horizontal axis*), with trajectories for sample ions that eventually gain energy $\sim 6 \times E_{\rm inj}$, for the $M_R = 20$, $M_A = 10.5$ case.

$$E' = E\left(\frac{m'L'^2T'^{-2}}{mL^2T^{-2}}\right). \quad (3)$$

It then follows from equations (1), (2), and (3) that

$$\Delta E' = \Delta E \frac{m'}{m}\left(\frac{v'_{\rm inj}}{v_{\rm inj}}\right)^2. \quad (4)$$

Defining the injection kinetic energy $E_{\rm inj} = mv_{\rm inj}^2/2$, it follows, from equation (4), that

$$\frac{\Delta E'}{\Delta E} = \frac{E'_{\rm inj}}{E_{\rm inj}}. \quad (5)$$

If $\Delta E = 6E_{\rm inj}$ as observed in our PIC simulations, then $\Delta E' = 6E'_{\rm inj}$, where $E'_{\rm inj} = \frac{1}{2}m'v'^2_{\rm inj}$.

To test this inferred scaling we performed two additional simulations, varying the mass ratio and the injection speed while keeping all other parameters constant. In the first additional simulation the mass ratio was changed to $M_R = m_i/m_e = 40$, twice the original value, and in order to keep the same inflow speed a slightly higher Alfvénic Mach number of 14.5 was used (see § 3.3). The maximum final energies achieved, as the most energetic particles leave the foot region, is again $\sim 6E_{\rm inj}$. This implies that the energies achieved scale linearly with mass, suggesting that the energization mechanism should also scale linearly with mass (Figs. 7*b* and 7*c*).

To study scaling with inflow speed, a further simulation with twice the inflow speed was conducted. In order to leave all other parameters unchanged, an Alfvénic Mach number of 21 (twice the original value of 10.5) was used. Again the maximum energy increase is $\sim 6E_{\rm inj}$, showing that the acceleration mechanism also scales with the square of the inflow speed (Figs. 7*a* and 7*c*).

3.3. *Astrophysical Energies*

The simple scaling derived in § 3.2, and exhibited in our PIC simulation results (Fig. 7), allows us to estimate the initial energization for nonrelativistic ions at astrophysical shocks.

In the simulation discussed in detail here, to reduce computational run times we use an ion to electron mass ratio of $M_R = m_i/m_e = 20$; however, the real $M_R = 1836$. As previously noted, when increasing mass ratio but maintaining the inflow speed, the Alfvénic Mach number ($M_{\rm A}$) must also be increased: $M_{\rm A} = v_{\rm inj}/v_{\rm A}$, where $v_{\rm A}$ is the Alfvén speed and $v_{\rm A} = B(\mu_0\rho)^{-1/2}$, so that $M_{\rm A} \propto v_{\rm inj}(m_i)^{1/2}$. Thus, a shock with $M_{\rm A} = 10.5$ for $M_R = 20$, becomes a shock of $M_{\rm A} \simeq 100$ when M_R is scaled up to 1836.

This value of Alfvénic Mach number, together with a magnetic field of 1×10^{-7} T, and other parameters used in the simulation, are in the region of expected values for the interstellar medium around a supernova remnant (Ellison & Reynolds 1991). An inflow speed of around 2.5×10^7 m s^{-1} and an ion mass of $1836 \times m_e$ ($m_e = 9.1 \times 10^{-31}$ kg), together with an increase in energy on leaving the foot of around 6 times the initial inflow energy as in the results above, implies that the maximum energy of ions as they leave the foot is $\sim$16 MeV.

4. CONCLUSIONS

Treating the full kinetic problem of a supercritical quasi-perpendicular collisionless plasma shock, including the dissipation as given by electron kinetics, we find the same foot-ramp-overshoot structure as obtained by earlier hybrid code simulations that yield time-stationary shocks. However, the structure in our PIC simulations is fundamentally time dependent: for the parameters of interest here, no time-stationary shock solutions exist, and instead we observe cyclic reformation on ion cyclotron timescales. As a consequence, the shock generates a suprathermal population of ions at energies up to $6E_{\rm inj}$. These energies scale linearly with the mass ratio, and with the square of the inflow velocity; this follows since the spatiotemporal scales of the electromagnetic fields relevant to the energization are determined by the kinetics of the injected ions: $L = v_{\rm inj}/\omega_{ci}$, $T = 1/\omega_{ci}$. This is most clearly seen when the electromagnetic fields are cast in the form of a potential that varies on two separate spatiotemporal scales. Electron phase space holes (or equivalently ion acoustic caviton structures) occur on electron spatiotemporal scales; thus, the associated electron acceleration mechanisms also operate on these scales (Dieckmann et al. 2000; Schmitz et al. 2002a, 2002b). Conversely, as we have seen, the ion acceleration mechanism is governed by the low-frequency bulk $\phi(t)$ of the foot's potential well. This varies on the slower ion time and spatial scales, together with the shock reformation cycle. The precise nature of the ion acceleration mechanism remains to be determined; we refer to the Appendix for a discussion of the key ingredients.

The scaling of our PIC results from the artificially low mass ratio up to the true mass ratio, together with realistic parameters from astrophysical observation, suggests that accelerated ions leave the SNR shock foot region with energies of order 10–20 MeV. However, care should be taken with our scaling results: we are extrapolating for the mass ratio over orders of magnitude, whilst testing the simulation phenomenology only over a very small range. As computer resources expand these results should be checked for much larger mass ratios, whilst maintaining the run times in terms of ion cyclotron periods.

The physics underlying the shock reformation cycle also invites further investigation. Previous work (Shimada & Hoshino 2000; Schmitz et al. 2002a) has shown that an increase in plasma β, and consequently higher thermal speeds in the inflow, can act to cut off the nonthermal tails in the electron energy spectra. In this case the ion phase space structure in the foot region greatly simplifies, with the number of instabilities (thought to cause reformation) diminishing greatly. However, some form of reformation may still occur, and the consequences for ion energization are unknown.

The present simulations are conducted in a $1x3v$ geometry. Whilst the work of Lembège & Savoini (1992) shows no major differences for higher numbers of spatial dimensions, hybrid simulations in $2x3v$, for longer run times, show that the current that can now exist along the shock front can lead to current-driven instabilities (Winske & Quest 1988). These instabilities may act to change the shock structure in the y-direction and so alter ion and electron dynamics across the shock front, affecting both ion and electron acceleration.

The plasmas simulated in our simulations are pure hydrogen, in that there are only two species—protons and electrons. The addition of other ion species would enable the shock acceleration of heavier ions to be simulated, together with the effects of heavy ions, with their different cyclotron scales, on shock reformation. Small percentages of heavy ions would also make the simulated environment more realistic. These will be the subject of further work.

R. E. L. acknowledges a CASE Research Studentship from the UK Particle Physics and Astronomy Research Council in association with UKAEA. This work was also supported in part by the UK Engineering and Physical Sciences Research Council. The computing facilities were provided by the Centre for Scientific Computing of the University of Warwick with support from Joint Research Equipment Initiative grant JR00WASTEQ.

APPENDIX

ELECTRIC POTENTIAL ON ION SCALES

Resolving the full electron and ion kinetics in the PIC code establishes two distinct spatiotemporal scales on which processes can occur. On fast timescales and short length scales there are, for example, plasma oscillations, that lead to fluctuations in charge density. However, on longer spatiotemporal scales the plasma is quasi-neutral but still supports bulk electric fields. We can obtain an expression for these by treating the plasma as two fluids, ions and electrons (for a treatment of more than two fluids see Chapman & Dunlop 1986; Chapman & Schwartz 1987), with equations of momentum conservation

$$n_e m_e \frac{D\boldsymbol{v}_e}{Dt} = -en_e(\boldsymbol{E} + \boldsymbol{v}_e \wedge \boldsymbol{B}) - \nabla P_e - n_e \nu_{ei} \boldsymbol{v}_e, \tag{A1}$$

$$n_i m_i \frac{D\boldsymbol{v}_i}{Dt} = q_i n_i(\boldsymbol{E} + \boldsymbol{v}_i \wedge \boldsymbol{B}) - \nabla P_i - n_i \nu_{ie} \boldsymbol{v}_i. \tag{A2}$$

The final terms in equations (A1) and (A2) represent collisional dissipation of momentum on the opposite plasma particle species. For example, in the notation, collisional momentum transfer from electrons to ions is represented by

$$n_e \nu_{ei} \boldsymbol{v}_e = \int m_e \boldsymbol{v} \left| \frac{\partial f_e}{\partial t} \right|_c d^3\boldsymbol{v}. \tag{A3}$$

We wish to consider time varying electromagnetic fields that only affect the ions, so that we can neglect ∇P_e and $\nu_{ei}\boldsymbol{v}_e$ on ion scales and take the limit in which the electrons respond instantaneously as a charge neutralizing fluid. This implies a vanishing electron inertial term, the "massless electron fluid" limit often used in hybrid codes:

$$m_e \frac{D\boldsymbol{v}_e}{Dt} \to 0. \tag{A4}$$

We can relate $\boldsymbol{v}_e$ directly to $\boldsymbol{v}_i$ via the current: on the spatiotemporal scales on which the electron-proton ($q_i = e$) plasma is quasi-neutral ($n_i \simeq n_e = n$), this reduces to

$$\boldsymbol{J} \simeq en(\boldsymbol{v}_i - \boldsymbol{v}_e). \tag{A5}$$

Substitution for $\boldsymbol{v}_e$ from equation (A5) into equation (A1) then gives

$$0 \simeq \boldsymbol{E} + \left[\boldsymbol{v}_i - \frac{\boldsymbol{J}}{en} \right] \wedge \boldsymbol{B}. \tag{A6}$$

Consistent with this low-frequency approximation we neglect the displacement current (the nonradiative limit), giving Ampère's law as

$$\nabla \wedge \boldsymbol{B} = \mu_0 \boldsymbol{J}. \tag{A7}$$

This implies the standard expression

$$\boldsymbol{J} \wedge \boldsymbol{B} = -\frac{1}{\mu_0} \left[\frac{\nabla B^2}{2} - (\boldsymbol{B} \cdot \nabla)\boldsymbol{B} \right]. \tag{A8}$$

Together, equations (A6) and (A8) yield

$$0 \simeq \boldsymbol{E} + \boldsymbol{v}_i \wedge \boldsymbol{B} + \frac{1}{\mu_0 en} \left[\frac{\nabla B^2}{2} - (\boldsymbol{B} \cdot \nabla)\boldsymbol{B} \right], \tag{A9}$$

which we can then invert to find $\boldsymbol{E}$ and the associated potential as follows.

In our one dimensional quasi-perpendicular geometry $\nabla \equiv (\partial_x, 0, 0)$, thus $(\boldsymbol{B} \cdot \nabla)\boldsymbol{B} = 0$, and $\phi(x,t) = \int E_x(x,t)dx$. Simplifying equation (A9) and taking the x component leads to

$$0 \simeq enE_x + en\left(v_{i,y}B_z - v_{i,z}B_y\right) + \frac{1}{\mu_0} \frac{\partial (B^2/2)}{\partial x}. \tag{A10}$$

To further simplify the problem we note that generally in our simulations, $B_y \ll B_z$ and $v_z \ll v_y$, thus $(v_{i,y}B_z - v_{i,z}B_y) \simeq v_{i,y}B_z$ and $B^2 \simeq B_z^2$ (recall $B_x = \text{const.}$). Then equation (A10) becomes

$$0 \simeq en(E_x + v_{i,y}B_z) + \frac{1}{\mu_0}\frac{\partial(B_z^2/2)}{\partial x}, \tag{A11}$$

and hence,

$$E_x \simeq -\frac{1}{en\mu_0}\frac{\partial(B_z^2/2)}{\partial x} - v_{i,y}B_z, \tag{A12}$$

where E_x is the x component of the electric field on the slow ion time and spatial scales on which the plasma is quasi-neutral.

The y component of equation (A9) yields the convective electric field

$$E_y \simeq v_{i,x}B_z. \tag{A13}$$

Substituting equation (A9) into equation (A2) leads to a simplified ion momentum equation:

$$nm_i\frac{D\boldsymbol{v}_i}{Dt} \simeq \frac{1}{\mu_0}\frac{\nabla B^2}{2} - \nabla P_i - n\nu_{ie}\boldsymbol{v}_i. \tag{A14}$$

Taking only the x component of equation (A14) leads to

$$\left|nm_i\frac{D\boldsymbol{v}_i}{Dt}\right|_x \simeq \frac{1}{\mu_0}\frac{\partial(B_z^2/2)}{\partial x} - \frac{\partial P_i}{\partial x} - n\nu_{ie}v_{i,x}. \tag{A15}$$

Thus, the bulk potential $\phi(x,t)$ seen by the ions is due to gradients in ion pressure and in magnetic field pressure.

The precise nature of the ion acceleration mechanism awaits detailed evaluation of $\boldsymbol{E}\cdot\boldsymbol{v}$ along particle orbits, which will be studied in forthcoming work. However, it is clear that its key elements are ion motion, including reflection and trapping, in the time evolving generalized potential $\phi(t)$; the x and y components of the convective electric field arising from this motion with respect to time varying B_z; and the contribution to E_x from the component of $\phi(t)$ that depends on ∇B_z^2.

REFERENCES

Bell, A. R. 1978, MNRAS, 182, 147
Bessho, N., & Ohsawa, Y. 1999, Phys. Plasmas, 6, 3076
Birdsall, C. K., & Langdon, A. B. 1991, Plasma Physics via Computer Simulation (London: Inst. Phys. Publ.)
Burgess, D., Wilkinson, W. P., & Schwartz, S. J. 1989, J. Geophys. Res., 94, 8783
Chapman, S. C., & Dunlop, M. W. 1986, J. Geophys. Res., 91, 8051
Chapman, S. C., & Schwartz, S. J. 1987, J. Geophys. Res., 92, 11059
Devine, P. E., Chapman, S. C., & Eastwood, J. W. 1995, J. Geophys. Res., 100, 17189
Dieckmann, M. E., McClements, K. G., Chapman, S. C., Dendy, R. O., & Drury, L. O'C. 2000, A&A, 356, 377
Ellison, D. C., & Reynolds, S. P. 1991, ApJ, 382, 242
Enomoto, R., et al. 2002, Nature, 416, 823
Fermi, E. 1949, Phys. Rev., 75, 1169
Hockney, R. W., & Eastwood, J. W. 1981, Computer Simulations Using Particles (New York: McGraw-Hill)
Hoshino, M., & Lembège, B. 1995, Adv. Space Res., 15, 67
Jokipii, J. R. 1987, ApJ, 313, 842
Koyama, K., Petre, R., & Gotthelf, E. V. 1995, Nature, 378, 255
Lembège, B., & Savoini, P. 1992, Phys. Fluids B, 4, 3533
Leroy, M. M. 1983, Phys. Fluids, 26, 2742
Quest, K. B. 1985, Phys. Rev. Lett., 54, 1872
———. 1986, Adv. Space Res., 6, 33
Schmitz, H., Chapman, S. C., & Dendy, R. O. 2002a, ApJ, 570, 637
———. 2002b, ApJ, 579, 327
Scholer, M., Shinohara, I., & Matsukiyo, S. 2003, J. Geophys. Res., 108, 1014
Sckopke, N., Paschmann, G., Bame, S. J., Gosling, J. T., & Russell, C. T. 1983, J. Geophys. Res., 88, 6121
Shimada, N., & Hoshino, M. 2000, ApJ, 543, L67
Tidman, D. A., & Krall, N. A. 1971, Shock Waves in Collisionless Plasmas (New York: Wiley)
Winske, D., & Quest, K. B. 1988, J. Geophys. Res., 93, 9681